PNAS RESEARCH ARTICLE | NEUROSCIENCE

# Pattern dynamics and stochasticity of the brain rhythms

Clarissa Hoffman[a], Jingheng Cheng[b], Daoyun Ji[b,c], and Yuri Dabaghian[a,1]

Edited by Nancy Kopell, Boston University College of Arts and Sciences, Boston, MA; received October 29, 2022; accepted February 7, 2023

**Our current understanding of brain rhythms is based on quantifying their instantaneous or time-averaged characteristics. What remains unexplored is the actual structure of the waves—their shapes and patterns over finite timescales. Here, we study brain wave patterning in different physiological contexts using two independent approaches: The first is based on quantifying stochasticity relative to the underlying mean behavior, and the second assesses "orderliness" of the waves' features. The corresponding measures capture the waves' characteristics and abnormal behaviors, such as atypical periodicity or excessive clustering, and demonstrate coupling between the patterns' dynamics and the animal's location, speed, and acceleration. Specifically, we studied patterns of $\theta$, $\gamma$, and ripple waves recorded in mice hippocampi and observed speed-modulated changes of the wave's cadence, an antiphase relationship between orderliness and acceleration, as well as spatial selectiveness of patterns. Taken together, our results offer a complementary—mesoscale—perspective on brain wave structure, dynamics, and functionality.**

patterning | waveforms | hippocampus | learning and memory

## Significance

Waveforms are commonly described in terms of their instantaneous properties, which are agnostic of protracted behaviors, or their time-averaged characteristics, which highlight mean trends. The actual shapes and patterns of waves over finite timescales thus remain unexplored. We propose an approach that allows quantifying waveforms as single entities and attributing precise meaning to intuitive notions of waves' "regularity," "typicality," or "orderliness." Thus, it becomes possible to distinguish statistically mundane patterns from deviant ones and to capture transitions between pattern types. We use these instruments to demonstrate that patterns of hippocampal rhythms in mice are dynamically coupled to motor activity in both behavioral and spatial contexts, which offers a fresh perspective on hippocampal circuit dynamics and functionality.

Oscillations of the extracellular fields—the brain waves—are produced by synchronized activity of large neuronal ensembles (1). These waves are key sources of neurophysiological information about brain activity at various spatiotemporal scales: spiking of individual neurons, synchronized circuit-level computations, high-level cognitive processes, etc. Common approaches to studying brain waves can be broadly divided in two categories. The first is based on correlating instantaneous phases, amplitudes, and frequencies with parameters of cognitive, behavioral, or neuronal processes. For example, instantaneous phases of the $\theta$-wave (4 to 12 Hz) modulate neuronal spikings (2, 3), while the $\gamma$-waves' (30 to 80 Hz) amplitudes and frequencies link the synaptic and circuit dynamics (4–8). The second category of analyses is based on quantifying the brain waves' time-averaged characteristics, e.g., establishing dependencies between the mean $\theta$-frequency and the animal's speed (9, 10) or acceleration (11), linking rising mean $\theta$- and $\gamma$-power to heightened attention states (12–14), and so forth.

However, little work has been done to examine the waves' overall structure, e.g., the temporal arrangement of peaks and troughs or sequences of sharp wave ripples or spindles generated over finite periods. Yet, the physiological relevance of a brain wave's shape, or *morphology** (15), is well-recognized: Rigidly periodic or excessively irregular rhythms that contravene a certain "natural" level of statistical variability are suggestive of circuit pathologies (16–25) or may indicate external driving (26, 27). For example, the nearly periodic sequences of peaks shown on Fig. 1 *A* and *B* are common for $\theta$-waves but are perhaps too regular for the $\gamma$-waves. Conversely, the intermittent patterns on Fig. 1 *C* and *D* are unlikely to appear among $\theta$-waves but may occur among $\gamma$-waves or ripples. The series of clumping peaks shown on Fig. 1 *D* and *E* are usual for ripples and may highlight underlying neuronal events. On the other hand, the waveform on Fig. 1*F* may represent an episode of $\theta$-arhythmicity or mundane temporal disorder of higher-frequency waves.

It remains unclear, however, how to characterize these patterns impartially and quantify the intuitive notions of "regularity," "typicality," "orderliness," etc. Furthermore, since all brain waves exhibit a certain level of erraticness, it is unclear how justified the experiential, visceral classifications of the waveforms as "mundane" or "irregular" are. For example, might the patterns assessed as "not-$\theta$" on Fig. 1 actually be short-time fluctuations of otherwise regular $\theta$-waves? Would that be a structural peculiarity or an impossibility?

In the following, we address these questions by studying patterns of waves recorded in the CA1 region of mouse hippocampus, using two independent mathematical

*Throughout the text, terminological definitions and highlights are given in *italics*.

Author contributions: Y.D. designed research; C.H., D.J., and Y.D. performed research; C.H. and Y.D. contributed new reagents/analytic tools; C.H., J.C., D.J., and Y.D. analyzed data; and C.H., J.C., D.J., and Y.D. wrote the paper.

The authors declare no competing interest.

This article is a PNAS Direct Submission.



[1]To whom correspondence may be addressed. Email: Yuri.A.Dabaghian@uth.tmc.edu.

This article contains supporting information online at http://www.pnas.org/lookup/suppl/doi:10.1073/pnas.2218245120/-/DCSupplemental.

Published March 28, 2023.

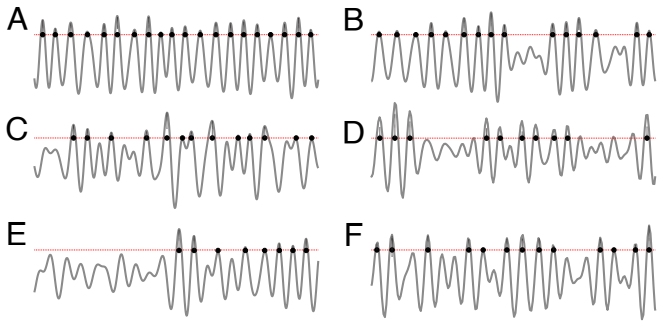


**Fig. 1.** Waveform morphologies. (*A* and *B*) Waves exhibiting nearly periodic sequences of peaks are commonly found among $\theta$-oscillations (4 to 12 Hz), but rarely among high frequency waves. The intermittent patterns shown on panels (*C*) or (*D*) may be exhibited by $\gamma$-waves (30 to 80 Hz), but for the $\theta$-waves, they would be atypical. The temporal clustering shown on panels (*D*) and (*E*) are all in all ordinary for $\gamma$- or ripples (150 to 250 Hz) but too irregular for the $\theta$-waves. *F*-pattern could potentially be a $\theta$-wave, a $\gamma$-wave, or a ripple. Shown are the peaks exceeding 1/2 of standard deviation from the mean (dashed red line), to exclude the spurious low-amplitude peaks. In actuality, panels *A* and *B* are experimental $\theta$-waveforms recorded from the mouse hippocampal CA1 (45, 46), panels *C* and *D* are the recorded $\gamma$-waves, and panels *E* and *F* show ripples.

frameworks, two cognate quantifications, which allow understanding the brain rhythms' structure at intermediate timescales and linking the wave patterns to the animal's behavior.

## 1. Approach

*1. Kolmogorov stochasticity*, $\lambda$, describes deviation of an ordered sequence, $X$, from the overall trend—in the following, $X$ will refer to the series of the brain waves' peaks, whose trend is defined by the expected mean rate of the peaks' appearance. A remarkable observation made in ref. 28 is that the $\lambda$-values are universally distributed. As it turns out, deviations, $\lambda(X)$, that are too high or too low are rare: sequences with $\lambda(X) \leq 0.4$ or $\lambda(X) \geq 1.8$ appear with probability less than 0.3%, Fig. 2 *A* and *B*, (29–34). In other words, typical patterns are consistent with the underlying mean behavior and produce a limited range of $\lambda$-values, with mean $\lambda^* \approx 0.87$. Thus, the $\lambda$-score can serve as a universal measure of *stochasticity* and be used for identifying statistical biases (or lack of thereof) in various patterns (35–40).

*2. Arnold stochasticity*, $\beta$, is alternative measure that quantifies whether the elements of a pattern (e.g., the aforementioned peaks) "repel" or "attract" each other. Repelling elements seek to maximize separations and hence produce orderly, more equispaced arrangements, for which $\beta$-stochasticity score is close to its minimum, $\beta(X) \approx 1$. On the other hand, attracting entities tend to cluster together, yielding patterns with higher stochasticity—their $\beta(X)$ can be as high as there are components in the sequence. Since both attraction and repulsion (any interaction, for that matter) contravene randomness, $\beta$-scores of sequences with independent elements are neither small nor large. As shown in ref. 41–44, $\beta$-scores of the sequences with independent elements are universally close to $\beta^* \approx 2$ (Fig. 2*C* and *Methods*). Thus, the $\beta$-score can be used to characterize *orderliness* of brain rhythms, complementing the $\lambda$-score.

*3. Time-dependence*. The recurrent nature of brain rhythms suggests a dynamic view on pattern stochasticity. Given a time window, $L$, containing a sequence of events, $X_t$, such as $\theta$-peaks or ripples, evaluate their scores $\lambda(X_t)$ and $\beta(X_t)$, then shift the window over a time step $\Delta t$, evaluate the next set $\lambda(X_{t+\Delta t})$ and $\beta(X_{t+\Delta t})$, and so on. The consecutive wave segments, obtained by small window shifts, $X_t, X_{t+\Delta t}, X_{t+2\Delta t}, \ldots$, differ only slightly from one another. Correspondingly, their stochasticity scores produce semicontinuous time dependencies $\lambda(t)$ and $\beta(t)$, which describe the dynamics of the waveforms over the signal's entire span (Fig. 2*D*).

For a visualization, one can imagine the elements of a given sample sequence, $X_{t+k\Delta t}$, as "beads" scattered over a necklace of length $L$. As the sliding window shifts forward in time, new beads may appear toward the front, as the beads in the back of the window disappear, while a majority of the beads retain their relative positions. The corresponding $\lambda$- and $\beta$-values will then produce semicontinuous dependencies $\lambda(t)$ and $\beta(t)$ that quantify the "necklace dynamics"—gradual pattern changes in time, with $\beta$ describing the orderliness of the beads' distribution and $\lambda$ measuring statistical typicality of the beads' ongoing arrangement (Fig. 2*D*).

As an illustration of the methods, consider simulated data series with random spacings between the adjacent values—

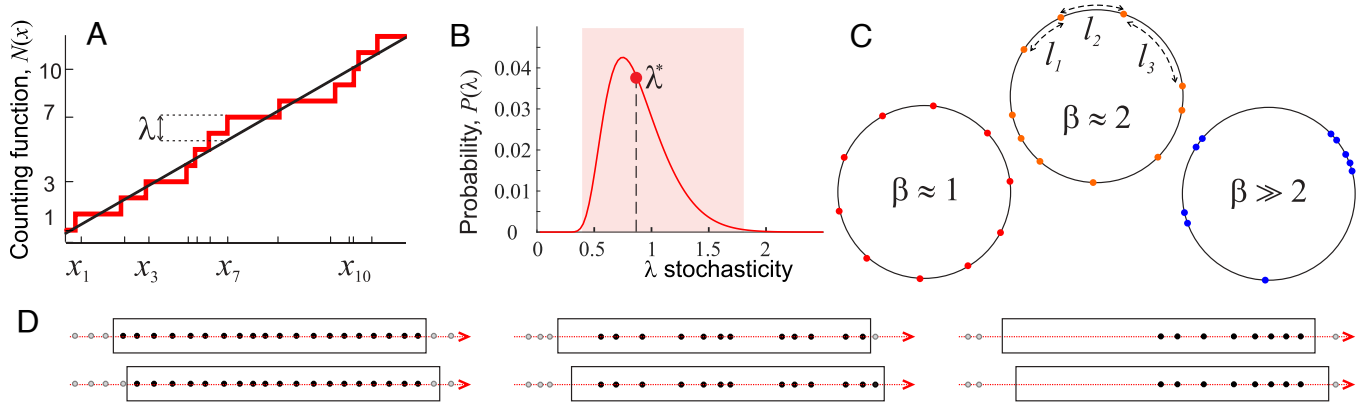


**Fig. 2.** Stochasticity parameters. (*A*) The elements of an ordered sequence $X = \{x_1, x_2, \ldots, x_n\}$ following a linear trend $\bar{N}(x) = \bar{f}x + b$ (solid black line). The sequence's maximal deviation from the mean, $\lambda(X)$, exhibits statistical universality and can hence impartially characterize the stochasticity of the individual data sequence $X$ (Section 3). (*B*) The probability distribution of $\lambda$-scores is unimodal, with mean $\lambda^* \approx 0.87$ (red dot). About 99.7% of all sequences produce $\lambda$-scores in the interval $0.4 \leq \lambda(X) \leq 1.8$ (pink stripe); these sequences are typical and consistent with the underlying mean behavior. In contrast, sequences with smaller or larger $\lambda$-scores are statistically uncommon. (*C*) A sequence $X$ arranged on a circle of length $L$ produces a set of $n$ arcs. The normalized quadratic sum of the arc lengths is small for orderly sequences, $\beta \approx 1$ (*Left*), as high as $\beta \approx n$ for the "clustering" sequences (*Right*), and intermediate, $\beta \approx 2$ (*Middle*), for generic sequences. (*D*) *Top* row: the "beads" of peaks illustrated on Fig. 1 *A*, *C*, and *E*. The black boxes represent time windows with widths scaled proportionally to the periods of $\theta$-waves, $\gamma$-waves and ripples. The gray dots represent the upcoming and the past peaks. *Bottom* row: time windows slide to the right (red arrows), causing pattern changes.

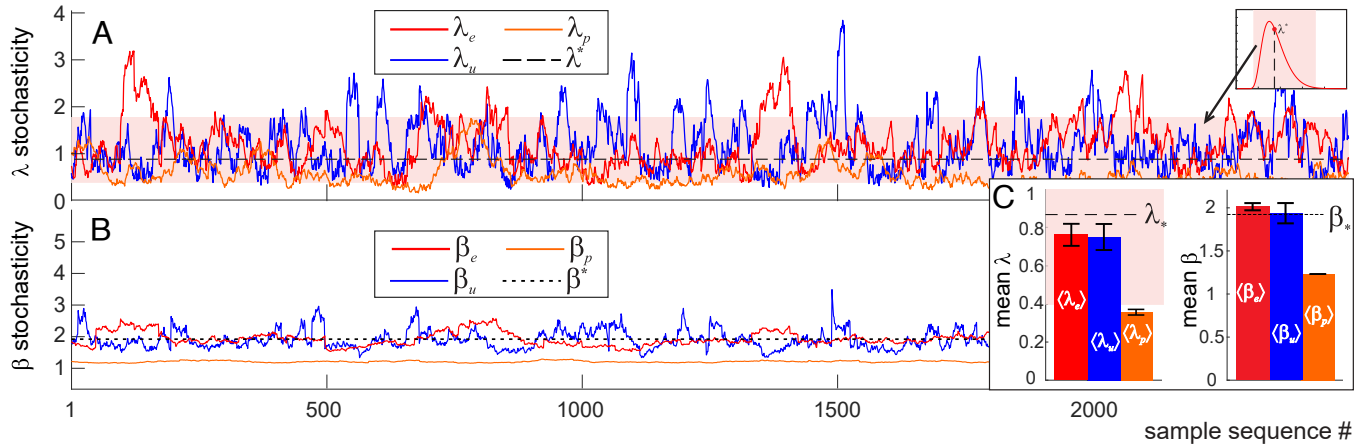


**Fig. 3.** Pattern dynamics for three kinds of random sequences in which the intervals between consecutive points are distributed 1) exponentially with the rate $\nu = 2$; 2) uniformly with constant density $\rho = 1$; or 3) with Poisson rate $\mu = 5$. Sample intervals are selected proportionally to the distribution scales ($L_U = 25\rho$, $L_e = 25\nu$, and $L_p = 25\mu$, so that each sample sequence contains about $n = 25$ elements) and are shifted by a single data point at a time. (*A*) The Kolmogorov parameter of the exponential sequence (red trace, $\lambda_e$), uniform sequence (blue trace, $\lambda_U$), and Poisson sequence (orange trace, $\lambda_p$) remains mostly within the "pink zone" of stochastic typicality (pink stripe is the same as on Fig. 2*B*, but stretched horizontally—note the illustration in the right corner). $\lambda_U$ is the most volatile and often escapes the expected range, whereas $\lambda_p$ is more compliant, lingering below the expected mean $\lambda_p \lesssim \lambda^* \approx 0.87$ (black dashed line). (*B*) The corresponding Arnold stochasticity parameters show similar behavior: $\beta_U = 1.93 \pm 0.2$ fluctuates around the expected mean $\beta^*(25) = 1.92$ (black dotted line). The exponential sequence has smaller $\beta$-variations and a slightly higher mean, $\beta_e = 2 \pm 0.04$. The Poisson sequence is the least stochastic (nearly periodic), with $\beta_p = 1.22 \pm 0.004$, due to statistical suppression of small and large gaps. (*C*) The mean stochasticity scores, $\langle\lambda\rangle$ and $\langle\beta\rangle$ computed for about $10^4$ random patterns of each type. For sample patterns, (*SI Appendix*, Fig. 1*A*).

intervals drawn from the familiar exponential, uniform, and Poisson distributions, with sample patterns containing about 25 consecutive elements. As shown on Fig. 3 *A* and *C*, the $\lambda(t)$-dependence of the exponential sequences remains, for the most part, constrained within the "typicality band" (pink stripe on Figs. 2*B* and 3*A*), while the uniformly distributed patterns are more variable, and the Poisson patterns follow the mean most closely. The $\beta$-scores of exponentially and uniformly distributed patterns are overall mundane, while the Poisson patterns exhibit periodic-like orderliness.

The mean $\lambda$- and $\beta$-scores in the uniform and exponential sequences are close to the universal means, $\lambda^*$ and $\beta^*$, which shows that, on average, they are statistically unbiased. In contrast, the Poisson-distributed patterns are atypically orderly, due to statistically suppressed small and large gaps between neighboring elements (Fig. 3*B*). Also, note that the fluctuations of stochasticity scores—the rises and drops of $\lambda(t)$ and $\beta(t)$ on Fig. 3—are chancy, since random sequences vary sporadically from instantiation to instantiation. In contrast, brain wave patterns carry physiological information, and therefore, the dynamics of their stochasticity is coupled with behavior and with physiological states, as discussed below.

## 2. Results

**A. Stochasticity in Time.** We analyzed Local Field Potentials (LFP) recorded in the hippocampal CA1 area of wild-type male mice for experimental details see refs. 45 and 46 and studied patterns of their $\theta$-waves, $\gamma$-waves, and ripples (47). The recurring nature of brain rhythms implies that their key features distribute uniformly over sufficiently long periods. The expected mean used for evaluating the Kolmogorov $\lambda$-parameter is hence linear,

$$\bar{N}(t) = \bar{f}t + b, \qquad [1]$$

with the specific coefficients $\bar{f}$ (the mean frequency) and $b$ obtained via linear regression. The lengths of the sample sequences were selected to highlight a particular wave's structure and functions, as described below.

**1. $\theta$-Waves** 4 to 12 Hz, (48, 49) are known to correlate with the animal's motion state, which suggests that the sample sequences should be selected at a behavioral scale (9–11). In the analyzed experiments (45, 46), the mice shuttled between two food wells on a U-shaped track, spending about 22 secs per lap (average for 5 mice, for both inbound and outbound runs) and consumed food reward over 17 s (Fig. 4*A*). On the other hand, the intervals between successive $\theta$-peaks distribute around the characteristic $\theta$-period, $\overline{T}_\theta \approx 1/\bar{f}_\theta \approx 110$ msecs, which defines the timescale of oscillatory dynamics (Fig. 4*B*). To accommodate both timescales, we used time intervals required to complete $1/6^{\text{th}}$ of the run between the food wells, $L_\theta \approx 3.6$ s, containing about 20 to 30 peaks—large enough to produce stable $\lambda$- and $\beta$-scores (50–52), but short enough to capture the ongoing dynamics of $\theta$-patterns.

*Fast moves.* As mentioned above, the experimental design enforces recurrent behavior, in which speed goes up and down repeatedly as the animal moves between the food wells. When the mouse moves methodically (lap time less than 25 s), $\lambda_\theta$ rises and falls along with the speed with surprising persistence (Fig. 4*C* and *SI Appendix*, Fig. 1*B*). Yet, the $\theta$-patterns appearing in this process are stochastically generic—the entire sequence of $\lambda_\theta$-values remains mostly within the "domain of stochastic typicality" (pink stripe on Figs. 4 *C* and *D* and 2*B*), below the universal mean $\lambda^*$. However, the patterns become overtly structured as the animal slows down: the Kolmogorov scores then drop below $\lambda_\theta \approx 0.1$, exhibiting uncommon compliance of the $\theta$-wave with the mean behavior. Such values of $\lambda_\theta$ can occur by chance with vanishingly small probability $\Phi(0.1) < 10^{-17}$ (Section 3), which, together with small $\beta_\theta \approx 1$, show that limited motor driving confines $\theta$-wave to a simple, nearly harmonic oscillation with a base frequency $\bar{f}_\theta \approx 9$ Hz.

Increasing speed drives $\theta$-patterns farther from the mean: the faster the mouse moves, the higher the $\lambda_\theta$. To quantify the uncanny similarity of the stochasticity to the speed profile,

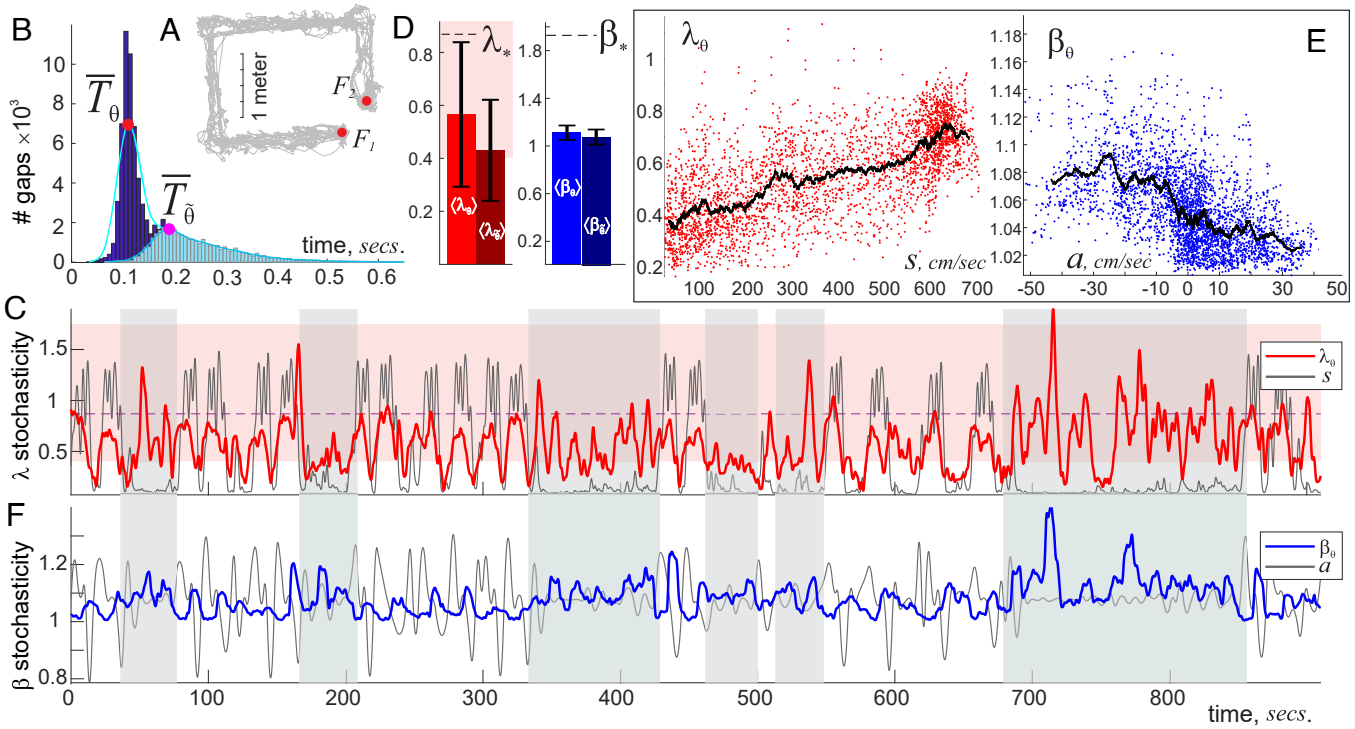


**Fig. 4.** $\theta$-wave's stochasticity. (*A*) The animal's lapses (trajectory shown by gray line) between food wells, $F_1$ and $F_2$, take on average 22 s. (*B*) A histogram of intervals between subsequent $\theta$-peaks concentrates around the characteristic $\theta$-period, $\overline{T}_\theta \approx 110$ ms: gaps shorter than $\overline{T}_\theta/2$ or wider than $2\overline{T}_\theta$ are rare. $\theta$-amplitude, $\tilde{\theta}$, oscillates with $T_{\tilde{\theta}} \approx 180$ ms period. (*C*) The dynamics of $\lambda_\theta(t)$ (red trace) correlate with the speed profile (gray line) when the mouse moves methodically. The $\lambda_\theta(t)$-stochasticity remains mostly within the "typical" range (pink stripe in the background), falling below it as the mouse slows down. For rapid moves there is a clear similarity between the $\lambda_\theta$-score and the speed, e.g., their peaks and troughs roughly match. When the mouse meanders (vertical gray stripes), the coupling between speed and $\lambda_\theta$-stochasticity is lost. (*D*) Due to quasiperiodicity of the $\theta$-wave and of its envelope, $\tilde{\theta}$, the average scores $\langle\lambda_\theta\rangle$, $\langle\lambda_{\tilde{\theta}}\rangle$, $\langle\beta_\theta\rangle$, and $\langle\beta_{\tilde{\theta}}\rangle$ are significantly lower than the impartial means $\lambda^*$ and $\beta^*$, with small deviations (data for 5 mice). (*E*) Locally averaged $\hat{\lambda}_\theta$-score grows with speed, whereas $\hat{\beta}_\theta$ tends to drop down with acceleration. (*F*) The Arnold score $\beta_\theta(t)$ (blue trace) remains close to $\beta_{\min} = 1$, affirming $\theta$-wave's quasiperiodicity. Note the antiphasic relationship between the $\beta_\theta$-stochasticity and the acceleration $a(t)$ (the latter graph is shifted upward to match the mean level $\langle\beta_\theta\rangle$): $\theta$-periodicity loosens as the animal slows down ($\beta_\theta$-splashes correlate with animal's deceleration) and sharpens as he speeds up.

we used the Dynamic Time Warping (DTW) approach. This technique uses a series of local stretches to match two functions—in this case, $\lambda_\theta(t)$ and $s(t)$—so that the net stretch can be interpreted as a measure of separation, or distance[†] between functions in "feature space" (54, 55). In our case, the DTW-distance between the speed and the $\lambda_\theta(t)$-score during active moves is small, $D(\lambda_\theta, s) = 19.6\%$, indicating that $\theta$-patterns are strongly coupled to the animals' motor mobility (*SI Appendix*, Fig. 2).

Note that DTW-affinity between $\lambda_\theta(t)$ and speed does not necessarily imply a direct functional dependence. Indeed, plotting points with coordinates $(s, \lambda_\theta)$ yields scattered clouds, suggesting a broad trend, rather than a strict relationship (Fig. 4*E*). However, if the $\lambda$-scores and the speeds are *locally averaged*, i.e., if each individual $s$- and $\lambda$-value is replaced by the mean of itself and its adjacents, then the pairs of such *local means* $(\hat{s}_i, \hat{\lambda}_i)$ reveal the underlying dependence: Increasing speed of the animal entails higher variability of the $\theta$-patterns.

In the meantime, the Arnold stochasticity score, $\beta_\theta(t)$, is closely correlated with the mouse's acceleration, $a(t)$. As shown on Fig. 4*F*, the $\beta_\theta$-score rises as the mouse decelerates ($\theta$-wave clumps) and falls when he accelerates ($\theta$-wave becomes more orderly), producing a curious antiphasic $\beta_\theta$-$a$ relationship, which is also captured by the local averages $(\hat{a}_i, \hat{\beta}_i)$ (Fig. 4*E*). The distance between $\beta_\theta(t)$ and $-a(t)$ (the minus sign accounts for the antiphase) is $D(\beta_\theta, -a) = 33.6\%$, which means that speed influences the $\theta$-wave's statistical typicality more than acceleration impacts its orderliness.

*Slow moves*. When the mouse meanders and slows down (lapse time over 25 s), $\theta$-patterns change: the $\lambda_\theta$-score increases in magnitude and uncouples from speed (DTW distance is twice that of the fast moves case, $D(\lambda_\theta, s) = 38.8\%$), suggesting that, without active motor driving, $\theta$-rhythmicity is less controlled by the mean oscillatory rate, i.e., is more randomized. The Arnold parameter $\beta_\theta$ also slightly increases, $D(\beta_\theta, -a) = 36.1\%$, indicating concomitant $\theta$-disorder.

Overall, the Kolmogorov scores of $\theta$-patterns are low, with mean $\langle\lambda_\theta\rangle = 0.54 \pm 0.12$, indicating that, on average, $\theta$-cycles closely follow the prescribed trend [**1**]. The low mean Arnold score $\langle\beta_\theta\rangle = 1.1 \pm 0.03 \approx \beta^{\min}$ also points at a near-periodic behavior of the $\theta$-wave (Fig. 4*C*). One may wonder, therefore, whether such structural rigidity should be viewed as a mere background that modulates the "true" $\theta$-stochasticity—the deviations of the $\theta$-wave from periodicity. In other words, one can view the times of the $\theta$-peaks' occurrences, $t_{\theta,k}$, as a periodic series disturbed by arrhythmic inputs, $t_{\theta,k} = k\bar{T}_\theta + \xi_{\theta,k}$, and inquire about the stochasticity of the latter. Expectedly, the "bare noise" patterns are more variegated: the $\lambda_\xi$-scores cover the full range of stochastic typicality, reflecting generic nature of the $\theta$-flickery (*SI Appendix*, Fig. 3*A*). The orderliness, $\beta_\xi(t)$, also grows significantly above the impartial mean $\beta^* \approx 2$, exposing cluttering of the $\theta$-fluctuations (*SI Appendix*, Fig. 3*B*). What is surprising however, it is that the $\xi_\theta$-patterns show no

[†]DTW separation typically satisfies the triangle inequality, $D(a,b)+D(b,c) \geq D(a,c)$, which permits interpreting it geometrically, as a distance between signals (53).

coupling to the speed, acceleration, or the physiological state, in contrast to the original $\theta$-wave. This observation is essential: It demonstrates that the semiperiodicity of the $\theta$-waveforms is, in fact, instrumental for linking $\theta$-patterns to movement activity.

The overall conclusion is that, during active behavior, $\theta$-waveforms are strongly controlled by the mouse's moves. Highly ordered, nearly periodic $\theta$-peaks appear when the animal starts running, i.e., the $\theta$-frequency range narrows, while deviating from the expected value. Decreasing speed stirs up the $\theta$-patterns; the disorder grows and reaches its maximum when the animal moves slowest and begins to accelerate. During periods of inactivity, the coupling between $\theta$-patterns and speed is weakened but then reinforced again as the mouse reengages into the task.

We emphasize that these dependencies should not be viewed as naive manifestations of known couplings between the waves' instantaneous or time-averaged parameters and the animals' activity (10, 11). Indeed, the momentary frequencies or amplitudes are agnostic of the wave's protracted behaviors and alter many times over the span of each extended peak series (56, 57). In contrast, the stochasticity scores describe the waveform as a single entity, without averaging, i.e., sensitive to the individual elements and features.

To further illustrate this point, we evaluated cross-correlation $R$ between the $\lambda_\theta$-score and the animal's speed during the active moving periods, which show that the similarity is highest when speed just barely lags behind $\lambda_\theta$, on average by $\delta t_\theta \approx 0.6$ s ($R_\theta = 0.6 \pm 0.02$). Getting ahead of the upcoming discussions, the highest correlation with the $\lambda_\gamma$ (stochasticity of the $\gamma$-wave) is also achieved when the speed lags by about $\delta t_\gamma = 0.45$ s ($R_\gamma = 0.51 \pm 0.15$). In contrast, the strongest correlation with $\lambda_{re}$ (stochasticity of the ripple waves, $R_{re} = 0.69 \pm 0.03$) may occur for leading speeds. The $\beta_\theta$-score shows similar range of maximal correlations with acceleration ($R_* \approx 0.5$), but with a wider spread of time shifts ($0 \lesssim \delta t_* \lesssim 1.5$ s), also with positive or negative lags. A similar variety of lagging and leading correlations are observed between the stochasticity scores and the waves' amplitudes and frequencies. Taken together, these observations suggest that the waveforms are neither spontaneous field deflections nor immediate reactions to ongoing idiothetic inputs but rather integrative processes that unfold at the behavioral timescale. The $\lambda$- and $\beta$-scores describe these waveforms integrally and put each pattern, as a whole, into a statistical perspective. It hence becomes possible to approach the questions addressed in the Introduction: identify typical and atypical wave patterns, quantify levels of their orderliness, detect deviations from natural behavior, and so forth.

**2. $\gamma$-waves** 30 to 80 Hz, (6) exhibit a wider variety of patterns than $\theta$-waves. The interpeak intervals between consecutive $\gamma$-peaks, $T_\gamma$, are nearly exponentially distributed, which implies that both smaller and wider $\gamma$-intervals are statistically more common, leading to higher pattern variability (Fig. 5*A*).

*Fast moves.* For consistency, the sample sequences, $X_\gamma$, were drawn from the same time windows, $L_\gamma = L_\theta \approx 3.6$ s, which contained, on average, about 100 elements that yield a mean Kolmogorov score $\langle\lambda_\gamma\rangle = 1.84 \pm 1.03$—more than twice higher than the impartial mean $\lambda^*$ and three times above the $\langle\lambda_\theta\rangle$ score. Such means can occur randomly with probability $1 - \Phi(1.84) \lesssim 2 \cdot 10^{-3}$, which suggests that generic $\gamma$-patterns are statistically atypical and may hence reflect organized network

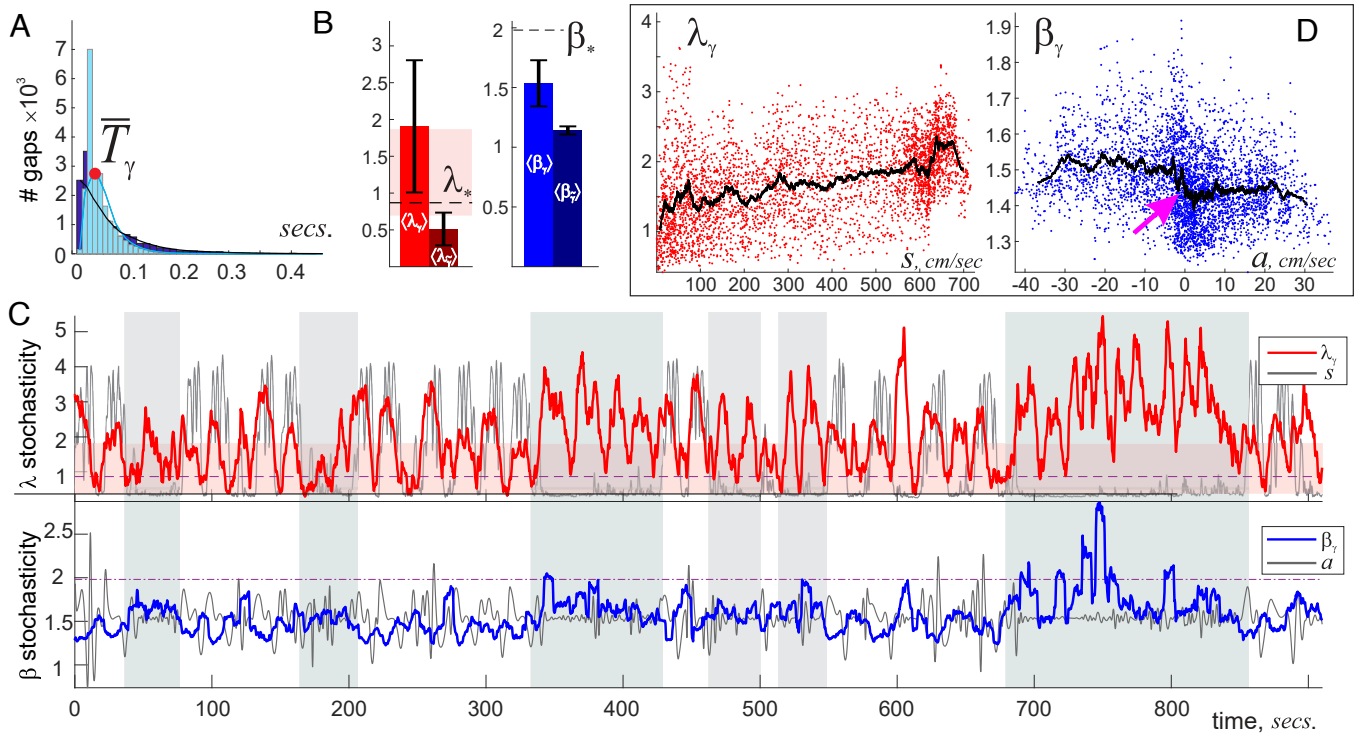


**Fig. 5.** $\gamma$-wave stochasticity. (*A*) A histogram of $\gamma$-interpeak intervals exhibits an exponential-like distribution with mean characteristic $\gamma$-period, $\overline{T}_\gamma = 18.6 \pm 1.9$ ms, about six times smaller than $\overline{T}_\theta$. (*B*) The average scores $\langle\beta_\gamma\rangle$ and $\langle\lambda_\gamma\rangle$ are higher than for the $\theta$-wave, indicating that $\gamma$-patterns are more diverse than $\theta$-patterns. (*C*) The dynamics of the $\lambda_\gamma$-score (*Top* panel) correlate with changes in the speed when the animal moves actively. Note that $\lambda_\gamma$ often exceeds the upper bound of the "pink stripe," i.e., $\gamma$-waves often produce statistically uncommon patterns, especially during rapid moves. The $\beta_\gamma$-score (*Bottom* panel) correlates with the animal's acceleration, which is lost when lap times increase (gray stripes). (*D*) Locally averaged $\lambda$-score, $\hat{\lambda}_\gamma$, grows with speed, while $\hat{\beta}_\gamma$ switches from higher to lower value with increasing acceleration (pink arrow).

dynamics, rather than random extracellular field fluctuations (Fig. 5*B*). The average Arnold parameter also grows compared to the $\theta$-case, but remains lower than the impartial mean, $\langle\beta_\gamma\rangle = 1.61 \pm 0.53 < \beta^*$, implying that, although $\gamma$-waves are more disordered than the $\theta$-waves, they remain overall oscillatory.

On average (for all five mice), the $\lambda_\gamma$-score escapes the domain of "stochastic typicality" approximately half of time through transitions that closely follow speed dynamics. A wider $\gamma$-diversity (larger range of $\lambda_\gamma$-values) is accompanied by a weaker coupling to speed: The average DTW distance to the latter, $D(\lambda_\gamma, s) \approx 23.4\%$, is slightly bigger than in the case of $\lambda_\theta$ dynamics, which illustrates that $\gamma$-patterns are less sensitive to speed than $\theta$-patterns (Fig. 5*C*).

From a structural perspective, the $\gamma$-wave becomes closer to periodic when the animal is actively moving: during these periods, $\beta_\gamma$-score reduces close to minimum, $\beta_\gamma \approx 1$, and the Kolmogorov score grows to the improbable $\lambda_\gamma \approx 3.5$ (cumulative probability of that is $\Phi(3.5) \lesssim 10^{-10}$). In contrast, the lowest deviations of $\gamma$-patterns from the mean ($\lambda_\gamma \gtrsim 0.2$), accompanied by high $\beta_\gamma$-scores, happen as the mice slow down, implying that circuit activity is least structured during these periods (Fig. 5 *C* and *D*). The relation between $\gamma$-orderliness, $\beta_\gamma(t)$, and acceleration is similar to the one observed in the $\theta$-waves: Acceleration induces stricter $\gamma$-rhythmicity and deceleration randomizes $\gamma$-patterns, with about the same overall DTW distance, $D(\beta_\gamma, -a) \approx 34.4\%$.

*During slower movements*, the $\gamma$-dynamics change qualitatively: the magnitudes of both $\lambda_\gamma(t)$ and $\beta_\gamma(t)$ grow higher, indicating that decoupling from motor activity enforces statistically atypical $\gamma$-rhythmicity in the hippocampal network, as in the $\theta$-waves. In particular, the uncommonly high $\beta_\gamma$-scores point at frequent $\gamma$-bursting during quiescence.

Once again, we emphasize that these results do not represent known correlations between instantaneous or time-averaged $\gamma$-characteristics and motion parameters (58, 59) but reflect the dynamics of $\gamma$-waves at pattern-changing timescale. Note in this connection that the amplitude of $\gamma$-waves, ($\gamma$-envelope, $\tilde{\gamma}$), has low stochasticity scores, comparable to the ones produced by the Poisson process, $\langle\beta_{\tilde{\gamma}}\rangle = 1.15 \pm 0.08$ and $\langle\lambda_{\tilde{\gamma}}\rangle = 0.52 \pm 0.26$ (Figs. 3 and 5*B*). In other words, instantaneous amplitudes and frequencies exhibit restrained, quasiperiodic behavior, and yet allow a rich morphological variety of the underlying $\gamma$-oscillations.

**3. Ripple events** (RE) High-amplitude (over 2.5 standard deviations above the mean) splashes of high-frequency waves 150 to 250 Hz (47), exhibit the richest pattern dynamics.

*During fast moves*, RE appears at an exponential rate $\overline{T}_{re} \approx 0.5$ s. Approximately, 20–30 RE occur in each 3.6-s window, which is comparable with the number of $\theta$-peaks over the same period, but RE have significantly higher $\lambda$-scores, $\langle\lambda_{re}\rangle = 2.40 \pm 1.57$ (Fig. 6 *A* and *B*). The low probability of these patterns ($1 - \Phi(2.4) \approx 10^{-4}$) and the relatively high mean $\beta$-score, $\langle\beta_{re}\rangle = 1.71 \pm 0.64$, indicate that RE tends to exhibit clustering that reflect time-specific, targeted circuit activity.

Interestingly, RE-patterns also correlate with the animal's speed profile about as much as $\gamma$-patterns, $D(\lambda_{re}, s) \approx 23.8\%$ (60). The $\beta_{re}(t)$-dependence displays the familiar antiphasic relationship with the animal's acceleration—RE tends to cluster more when the animal slows down (Fig. 6 *C* and *D*). However, orderliness of RE is driven by acceleration even stronger than

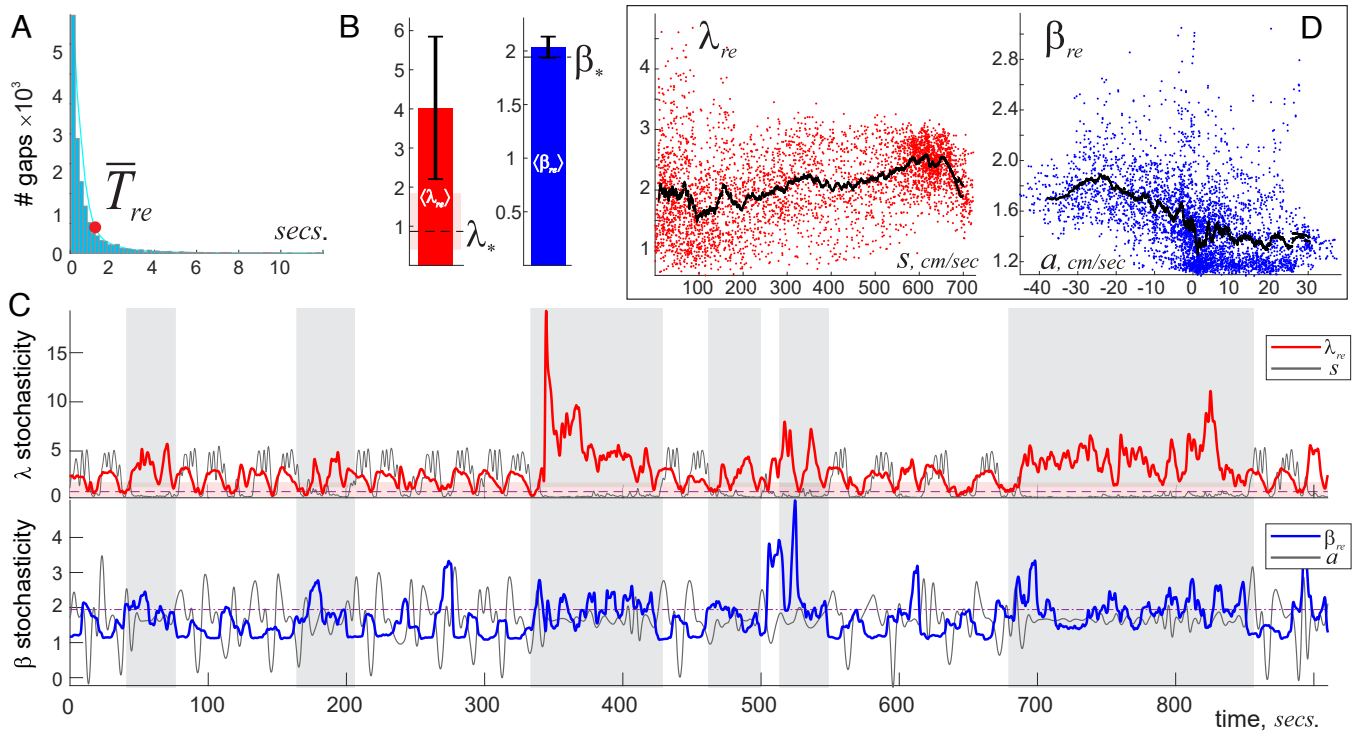


**Fig. 6.** Ripple Events' stochasticity. (*A*) A histogram of intervals between RE is nearly exponential. (*B*) The averages $\langle\lambda_{re}\rangle$ and $\langle\beta_{re}\rangle$ are high, indicating both frequent deviation of RE from the mean and higher temporal clustering than for the $\theta$- and $\gamma$-patterns. (*C*) The animal's speed (gray line, *Top* panel) correlates with the Kolmogorov parameter $\lambda_{re}$ during fast exploratory laps. During inactivity (vertical gray stripes), the $\lambda_{re}$-stochasticity uncouples from speed, exhibiting high spikes that mark strong "fibrillation" of RE patterns and may reflect awake replay activity. The antiphasic relationship between the animal's acceleration $a(t)$ (gray line, *Bottom* panel) and Arnold score $\beta_{re}(t)$ shows that RE tends to cluster when as the animal decelerates, while acceleration enforces periodicity. During slower moves (gray stripes), the relationship between speed, acceleration, and stochasticity is washed out and stochastically improbable patterns dominate. (*D*) Locally averaged $\hat{\lambda}_{re}$ grows with speed and $\hat{\beta}_{re}$ drops with acceleration.

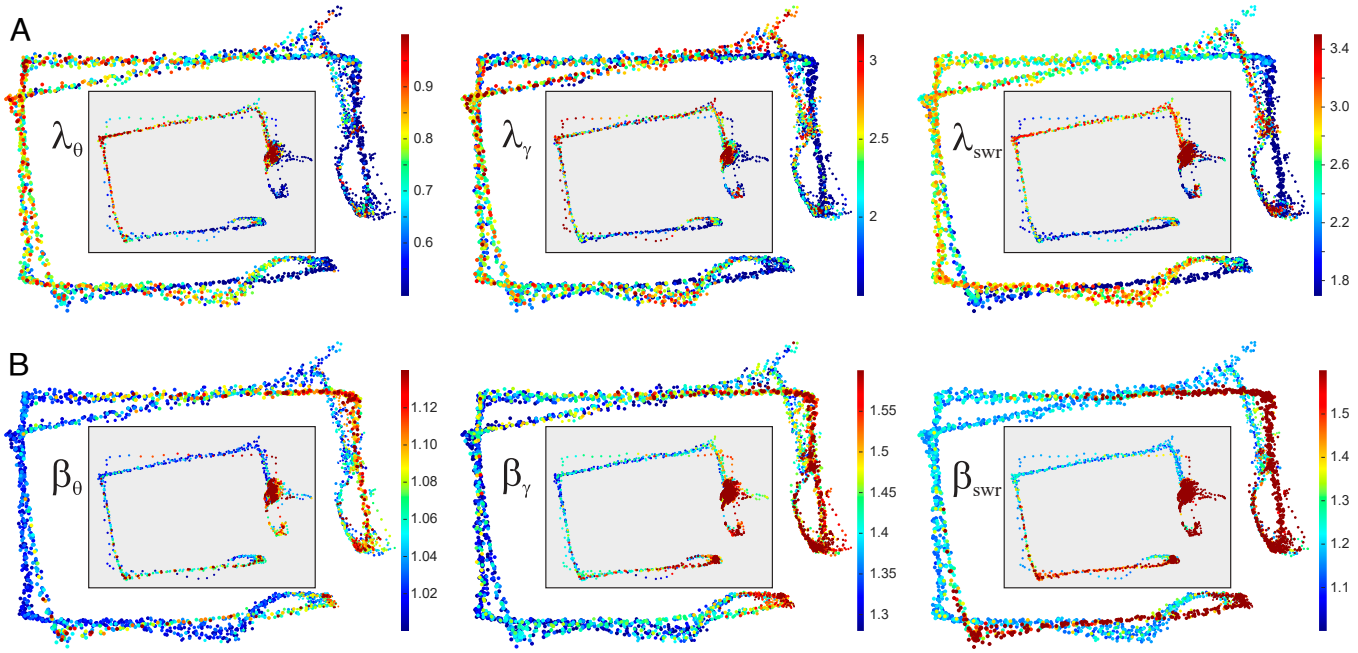


**Fig. 7.** Spatial stochasticity maps were obtained by plotting $\lambda$ and $\beta$ parameters along the trajectory. Note that the inbound and the outbound trajectories are slightly different, leading to two seemingly displaced tracks in each plot. (*A*) The $\lambda$-maps show that $\theta$-wave, $\gamma$-wave, and RE generally follow the mean trend near the food wells (with scattered wisps of high stochasticity) and deviate from the mean over the areas most distant from the food wells. The smaller maps in the gray boxes represent slow lapses: the overall layout of high-$\lambda$ and low-$\lambda$ fields is same as during the fast moves, which suggests spatiality of $\lambda$-stochasticity. (*B*) The behavior of $\beta_\theta$ is opposite: the "uneventful," distant run segments attract nearly periodic behavior, while the food wells attract time-clumping wave patterns. Note that, at the food wells, the waves exhibit highly improbable (high-$\lambda$), disordered (high-$\beta$) patterns.

orderliness of $\gamma$-patterns: the range of $\beta_{re}$-scores is twice as wide as the range of $\beta_\gamma$-scores (broader pattern variety), with a similar DTW distance $D(\beta_{re}, -a) \approx 39.7\%$.

*During quiescent periods*, RE are known to mark instances of endogenous network activity—sequential reactivations of hippocampal neurons that represent previous or future behavioral experiences—awake replays and preplays (60–66) no sleep periods involved, Section 3 and (45, 46). As shown on Fig. 6*C*, these RE patterns are highly uncommon: the extremely high $\lambda_{re}$-scores and above-average $\beta_{re}$-values indicate statistically improbable, clustered RE sequences.

Overall, the temporal clumping comes forth as a characteristic feature of the RE, suggesting that these phenomena are manifestations of fast network dynamics that brusquely "ripple" the extracellular field, unlike the rhythmic $\theta$ and $\gamma$ undulations (47).

Note that although stochasticity scores of different waves exhibit similar qualitative behaviors, e.g., all $\lambda$s grow with speed and all $\beta$s increase with acceleration, they remain largely independent from each other, e.g., $\lambda_\theta$ is independent from $\lambda_\gamma$, $\beta_\gamma$ does not depend on $\beta_{re}$, etc. (*SI Appendix*, Fig. 4). In other words, the results illustrated on Figs. 4, 5, and 6, are not redundant—they each provide a standalone description of the oscillatory dynamics in the corresponding frequency band.

**B. Stochasticity in Space.** Distributing the $\lambda$- and $\beta$-scores along the animal's trajectory yields *spatial maps of stochasticity* for each brain rhythm and reveals a curious spatial organization of LFP patterns with similar morphology. As shown on Fig. 7, higher $\lambda$-values for all waves are attracted to segments where the mouse is actively running with maximal speed, furthest away from the food wells. Patterns that are close to the expected average (low-$\lambda$) concentrate in the vicinity of food wells where the animal moves slowly. These regions also tend to host high $\beta$-scores that appear as the animal slows down to eat, as well as the lowest $\beta$s, which appear as the animal accelerates away (65). In other words, the LFP waves become more "trendy" and, at the same time, more structured (either more periodic or more clustered) over the behaviorally important places (e.g., food wells) that require higher cognitive activity. On the other hand, the outer parts of the track, where the brain waves are less controlled by the mean and remain moderately disordered, are marked by irregular patterns.

Intriguingly, the same map structure is reproduced during slow lapses, when the motor control of the patterns weakens, suggesting that speed and acceleration are not the only determinants of the LFP patterns. As shown on Fig. 7, even when the mouse dawdles, the waves tend to deviate from the mean around the outer corners and follow the mean in the vicinity of the food wells. Similarly, the patterns start clumping as the mouse approaches the food wells and distribute more evenly as he moves away.

These results suggest that spatial context may, by itself, influence hippocampal brain rhythm structure, in a way that is reminiscent of the place-specific activity of spatially tuned neurons in sectioned environments, e.g., place cells (67) or parietal neurons (68), which highlight geometrically similar domains (see also linearized maps, *SI Appendix*, Fig. 5). Specifically, the "bursting fields" (high-$\beta$) and "domains of regularity" (small $\lambda$) surround food wells; the "quasiperiodicity fields" (small $\beta$s) as well as "wobbling fields" (large $\lambda$s) stretch over the outer segments, notably corners (Fig. 7). Physiologically, spatiality of stochasticity may reflect a coupling between the hippocampal place-specific spiking activity and extracellular field oscillations.

## 3. Discussion

Recorded LFP signals are superpositions of locally induced extracellular fields and inputs transmitted from anatomically remote networks. The undulatory appearance of the LFP is often

interpreted as a sign of structural regularity[‡], but the dynamics of these rhythms is actually highly complex. Understanding the balance between deterministic and stochastic perspectives on LFPs pose significant conceptual challenges, as it happened previously in other disciplines (70).

Structurally, LFP rhythms may be described through discrete sequences of wave features (heights of peaks, specific phases, interpeak intervals, etc.) or viewed as transient series—bursts—of events, as in the case of REs (71). It is well-recognized that such sequences are hard to forecast, e.g., a recent discussion of a possible role of bursts in brain waves' genesis posits: *"An important feature that sets the burst scenario apart is the lack of continuous phase-progression between successive time points—and therefore the ability to predict the future phase of the signal—at least beyond the borders of individual bursts"* (71). In other words, the nonlinearity of LFP dynamics, as well as its transience and sporadic external driving, result in effective stochasticity of LFP patterns—an observation that opens a new round of inquiries (71, 72). For example, how exactly should one interpret the "unpredictability" of a temporal sequence? Does it mean that its pattern cannot be resolved by a particular physiological mechanism or that it is unpredictable in principle, "genuinely random," as, e.g., a gambling sequence? What is the difference between the two? Are the actual network computations based on "overcoming randomness" and somehow deriving the upcoming phases or amplitudes from the preceding ones or may there be alternative ways of extracting information? Does the result depend on the "degree of randomness" and if so, how to distinguish between "more random" and "less random" patterns? These questions are not technical, pertaining to a specific mechanism, nor specifically physiological; rather, these are fundamental problems that transcend the field of neuroscience. Historically, similar questions have motivated mathematical definitions of randomness that are still debated to this day (73–75).

The approach suggested by Kolmogorov in 1933 the year when brain waves were discovered (76) is based on the statistical universality of deviations from the expected behavior (28, 29). From Kolmogorov's perspective, randomness is contextual: if a sequence $X$ deviates from an expected mean behavior within bounds established by the distribution [**3**], then $X$ is *effectively* random. In other words, an individual sequence may be viewed as random if it could be randomly drawn from a large pool of similarly trending sequences, with sufficiently high probability. This view permits an important conceptual relativism: Even if a sequence is produced by a specific mechanism or algorithm, it can still be viewed as random as long as its $\lambda$-score is "typical" according to the statistics [**3**]. For example, it can be argued that geometric sequences are typically more random than arithmetic ones, although both are defined by explicit formulae (30–34). By analogy, individual brain rhythms may be generated by specific synchronization mechanisms at a precise timescale, and yet they may be empirically classified and quantified as stochastic.

A practical advantage of Kolmogorov's approach is that mean trends, such as [**1**], can often be reliably established, interpreted, and then used for putting the stochasticity of the underlying sample patterns into a statistical perspective. Correspondingly, assessments based on $\lambda$-scores were previously applied in a variety of disciplines from genetics (35–37) to astronomy (38) and from economics (39) to number theory (30–34, 40–44, 77). Some work has also been done in brain wave analyses, e.g., for testing normality of electroencephalograms' long-term statistics (78–81). Arnold $\beta$-score provides an independent assessment of orderliness (whether elements of an arrangement tend to attract, repel, or be independent of each other) and it has not been, to our knowledge, previously used in applications.

Importantly, Kolmogorov and Arnold scores are impartial and independent from physiological specifics or contexts, thus providing self-contained semantics for describing the LFP data and a novel venue for analyzing the underlying neuronal mechanisms. It becomes possible to distinguish "statistically mundane" LFP patterns from exceptional ones and to capture the transitions between them, as well as to link pattern dynamics to changes in the underlying network's dynamics. For example, since $\theta$-bursts are physiologically linked to long-term synaptic potentiation (82, 83), $\theta$-patterns with high $\beta$-scores may serve as markers of plasticity processes taking place in the hippocampal network at specific times and places (84–86). Furthermore, high-$\beta_\theta$ regions near food wells indicate that reward proximity may also trigger hippocampal plasticity and, since hippocampal neurons' spiking is coupled to $\theta$-cycles (2), have a particular effect on memory processing. On the other hand, low-$\beta_\theta$ indicates limit cycles in the network's phase space that uphold simple periodicity. $\gamma$-bursts (high $\beta_\gamma$) mark heightened attention and learning periods (5, 87). In our observations, they appear during the mouse's approach to the reward locations and disappear as it ventures away from them. Clustering ripples during quiescence reflect dense replay activity (61, 62), indicative of periods of memory encoding, retrieval, and network restructurings (63, 88).

Overall, the proposed approach allows studying brain rhythms from a new perspective that complements existing methodology, which may lead to a deeper understanding of the synchronized neuronal dynamics and its physiological functions.

## Materials and Methods

**Experimental Procedures.** The LFP data used in this study were previously analyzed via the conventional Fourier transformation method and published in refs. 45 and 46. Data were recorded from the CA1 pyramidal cell layer of hippocampus. The animals were trained in a familiar room to run back and forth on about ~2-m long rectangular track (Fig. 4*B*) for food reward. The daily recording procedure consisted of two sessions on the track, lasting about 15 min each, followed by one to two 15-min break in the sleeping box. The recording was repeated 3–10 d. The LFP data were sampled at 2 kHz rate. Two color diodes (red, green) were mounted over the animal's head to track its positions, sampled at 33 Hz with a resolution approximately 0.2 cm. Further details on surgery, tetrode recordings, and other procedures can be found in (45, 46).

**Computational Algorithms.** The following outline of mathematical methods is based on refs. 28–34, 41–44

*1. Kolmogorov score.* Let $X = x_1 \le x_2 \le \ldots \le x_n$, be an ordered sequence and let $N(X, L)$ be the number of elements smaller than $L$,

$$N(X, L) = \{\text{number of } 0 \le x_k < L\}.$$

Let $\bar{N}(X, L)$ be the expected number of elements that interval; in case of the brain rhythms, this number will grow proportionally to the length of the interval, with the slope defined by the rhythm's frequency (Fig. 8).

The closer $X$ follows the prescribed behavior, the smaller the normalized deviation[§]

$$\lambda(X) = \sup_L |N(X, L) - \bar{N}(X, L)|/\sqrt{n}. \qquad [2]$$

[‡] A succinct expression of this view is provided in 69: "*rhythmicity is the extent to which future phases can be predicted from the present one.*"

[§] The supremum, rather than maximum, is required in formula [**2**] due to discontinuity of the counting function $N(X, L)$ at the stepping points.

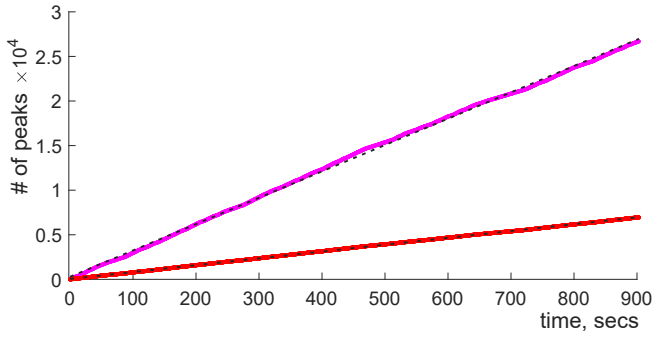


**Fig. 8.** Counting functions for $\theta$-peaks ($N_\theta$, red) and $\gamma$-peaks ($N_\gamma$, magenta) evaluated for one entire running session, for one mouse. The black lines show the estimated (95% prediction interval) linear trends.

A remarkable observation made in ref. 28 is that the cumulative probability of having $\lambda(X)$ smaller than a given $\lambda$ converges to the function

$$\Phi(\lambda) = \sum_{k=-\infty}^{\infty} (-1)^k e^{-2k^2\lambda^2}, \qquad [3]$$

that starts at $\Phi(0) = 0$ and grows to $\Phi(\infty) = 1$. The derivative of the cumulative density [**3**] defines the probability distribution for $\lambda$, $P(\lambda) = \partial_\lambda \Phi(\lambda)$ illustrated on Fig. 2*B* Even though the range of $P(\lambda)$ includes arbitrarily small or large $\lambda$s, the shape of the distribution implies that excessively high or low $\lambda$-values are rare, e.g., sequences with $\lambda(X) \le 0.4$ or $\lambda(X) \ge 1.8$ appear with probability less than 0.3%, $\Phi(0.4) \approx 0.003$, and $\Phi(1.8) \approx 0.997$. Since these statistics are universal, i.e., apply to any sequence $X$, the $\lambda$-score can serve as a universal measure of "stochastic typicality" of a pattern (29–34). This is akin to the familiar use of normally distributed $z$-scores: "typical" $z$s (99.7% of them) lay in the range $-3 \le z \le 3$, while small ($z < -3$) or large ($z > 3$) scores appear with probability 0.3%. Just as the $z$-scores are used to detect outliers in a normal distribution, $\lambda$-scores measure typicality of patterns: if a pattern $X$ deviates from the expected mean within limits established by the "hump" of the $P(\lambda)$-distribution (pink stripe on Fig. 2*B*), then $X$ is typical. If, however, these limits are surpassed, then the pattern is "atypical," "uncommon," "not chancy," and may be viewed as a sign of a severe trend violation, or a "trend change."

*2. Corrections to Kolmogorov score* up to the order $n^{-3/2}$,

$$\lambda(X) \to \lambda(X)\left(1 + \frac{1}{4n}\right) + \frac{1}{6n} - \frac{1}{4n^{3/2}}, \qquad [4]$$

allow increasing the accuracy of the finite-sample estimates to over 0.01% for sequences containing as little as 10 to 20 elements (50–52). In this study, all $\lambda$-evaluations are based on the expression [**4**] and use data sequences that contain more than 25 elements.

*3. Mean Kolmogorov stochasticity score*. The mean $\lambda$ can then be computed as

$$\lambda^* = \int_0^\infty \lambda P(\lambda) d\lambda = \int_0^\infty \Phi(\lambda) d\lambda,$$

where we used integration by parts and the fact that the distribution $P(\lambda)$ starts at 0, $P(0) = 0$, and approaches 0 at infinity, $P(\infty) = 0$ (Fig. 2*B*). Integrating the Gaussian terms in expansion [**3**] yields Mercator series

$$\lambda^* = \sqrt{\frac{\pi}{2}} \sum_{k=1}^{\infty} (-1)^{k+1} \frac{1}{k} = \sqrt{\frac{\pi}{2}} \ln 2 \approx 0.8687.$$

*4. $\Phi(\lambda)$ estimates*. For small $\lambda$s, the Kolmogorov $\Phi$-function [**3**] can be approximated by

$$\Phi(\lambda) \approx \frac{\sqrt{2\pi}}{\lambda} e^{-\pi^2/8\lambda^2}, \qquad [5]$$

and for large $\lambda$s, it is approximated by the two lowest-order terms in [**3**], $\Phi(\lambda) \approx 1 - 2e^{-2\lambda^2}$ (28, 29). These formulae allow quick evaluations of the $\lambda$-scores' cumulative probabilities outside of the "stochastic typicality band," $\lambda < 0.4$ or $\lambda > 1.8$.

*5. Arnold score*. Let us arrange the points of the sequence $X$ on a circle of length $L$ and consider the arcs between pairs of consecutive elements, $x_i$ and $x_{i+1}$ (Fig. 2*C*). If the lengths of these arcs are $l_1, l_2, \ldots, l_n$, then the sum

$$B = l_1^2 + l_2^2 + \ldots + l_n^2, \qquad [6]$$

grows monotonically from its smallest value $B_{\min} = n(L/n)^2 = L^2/n$, produced when the points $x_k$ lay equidistantly from each other, to its largest value, $B_{\max} = L^2$, attained when all elements share the same location, with the mean $B^* = B_{\min} 2n/(n+1) \approx 2B_{\min}$ (41–44).

Intuitively, orderly arrangements appear if the elements "repel" each other, "clumping" is a sign of attraction, while independent elements are placed randomly. Hence, the ratio $\beta = B/B_{\min}$ can be used to capture the orderliness of patterns:

$$\begin{cases} \beta(X) \approx 1, & \text{indicates atypically ordered, nearly equidistant sequences;} \\ \beta(X) \approx \beta^* \approx 2 & \text{marks statistically typical, commonly scattered sequences;} \\ \beta(X) \gg \beta^* & \text{corresponds to clustering sequences.} \end{cases} \qquad [7]$$

*6. The length L of the circle* accommodating a random sample sequence $X$ in Arnold's method was selected so that the distance between the end points, $x_0$ and $x_n$, became equal to the mean arc length between the remaining pairs of neighboring points,

$$l_n = |x_n - x_0| \mod L = \frac{1}{n-1} \sum_{i=1}^{n-1} l_i.$$

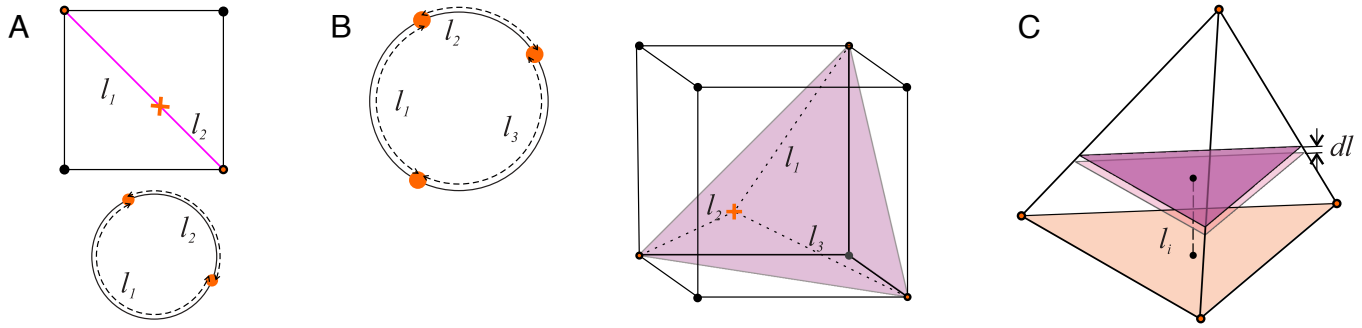


**Fig. 9.** Averaging over a simplex. (*A*) If two coordinates $l_1$ and $l_2$ of a two-element sequence could independently vary between 0 and $L$, then the pair $(l_1, l_2)$ would cover a 2*D* square. However, if the elements $(x_1, x_2)$ remain on a circle (orange dots below) then the Eq. **8** restricts $(l_1, l_2)$-values to the cube's diagonal (orange cross on the *Top* panel), i.e., to a 1-dimensional simplex. (*B*) A configuration of three points on a circle corresponds to a point on the diagonal section of a $L$-cube. (*C*) Tetrahedron—a section of a 4*D* cube—is the highest dimensional (3*D*) depictable simplex $\sigma^{(3)}$, which is used to schematically represent $n$-dimensional simplexes, $\sigma^{(n)}$. Averaging over $l_i^2$ in [**9**] involves integrating over it the $(n-1)$-dimensional layers of $\sigma^{(n)}$.

*7. Mean Arnold stochasticity score*. A short derivation of $\beta^*$ is provided below for completeness, following the exposition given in ref. 44.

- The $n$ arcs lengths $l_1, l_2, \ldots, l_n$ produced by $n$ points, $X = \{x_1, x_2, \ldots, x_n\}$, can be viewed as the "coordinates" of $X$ in a $n$-dimensional sequence space. If these coordinates could vary independently on a circle of length $L$, then the sequences would be in one-to-one correspondence with the points of a $n$-dimensional hypercube with the side $L$. However, since the sum of $l_i$s must remain fixed,

$$l_1 + l_2 + \ldots + l_n = L, \qquad [8]$$

the admissible $l$-values occupy a hyperplane that cuts between the vertices $(0, 0, \ldots, 0)$ and $(L, L, \ldots, L)$. For example, two values $l_1$ and $l_2 = L - l_1$ define a point on the diagonal of a $L$-square (Fig. 9*A*), three values define points of a "diagonal" equilateral triangle in the $L$-cube (Fig. 9*B*), four values represent points of a regular tetrahedron (Fig. 9*C*), and so forth. A generic $n$-sequence is hence represented by a point in a polytope spanned by $n$ vertices in $(n-1)$-dimensional Euclidean space–a $(n-1)$-*simplex*, $\sigma^{(n-1)}$ (89).
- The *defining property* of a simplex is that any subcollection of its vertices spans a subsimplex: a tetrahedron, $\sigma^{(3)}$, is spanned by four vertices, any three of which span a triangle $\sigma^{(2)}$–a "face" of $\sigma^{(3)}$; any two vertices span an edge, $\sigma^{(1)}$, between them, etc. (89). Correspondingly, a generic section of the $\sigma^{(n-1)}$-simplex by a hyperplane is also a $\sigma^{(n-2)}$-simplex (Fig. 9*C*).
- Averaging the sum [**6**] requires evaluating the mean of each $l_i^2$,

$$\langle l_i^2 \rangle = \frac{1}{V_{n-1}} \int_{\sigma^{(n-1)}} l_i^2 dV, \qquad [9]$$

for $i = 1, 2, \ldots, n$. Here, $V_{n-1}$ refers to the volume of $\sigma^{(n-1)}$ and "$dV$" refers to the volume of a thin layer positioned at a distance $l_i$ away from the $i$th face (Fig. 9*C*). By the defining property of simplexes mentioned above, the base of this layer is a $(n-2)$-simplex specified by the equation

$$\sum_{j \neq i}^{n} l_j = L - l_i,$$

which implies that the sides of this base have length $L - l_i$ just as the sides of $\sigma^{(n-1)}$ defined by [**8**] have length $L$. The volume of the thin layer is $dV = C(L - l_i)^{n-2} dl_i$, so that

$$\langle l_i^2 \rangle = \frac{C}{V_{n-1}} \int_0^L l_i^2 (L - l_i)^{n-2} dl_i = \frac{CL^{n+1}}{V_{n-1}} \int_0^1 u^2 (1-u)^{n-2} du,$$

where $u = l_i / L$. Using the variable $v = 1 - u$, the latter integral yields:

$$\langle l_i^2 \rangle = \frac{CL^{n+1}}{V_{n-1}} \int_0^1 (1-v)^2 v^{n-2} dv = C \left( \frac{1}{n-1} - \frac{2}{n} + \frac{1}{n+1} \right).$$

The volume of the $\sigma^{(n-1)}$-simplex is

$$V_{n-1} = \int_0^L dV = \frac{CL^{n-1}}{n-1};$$

hence the sum [**6**] divided by $B_{\min} = L^2/n$ yields

$$\langle \beta_n \rangle = n^2 \left( 1 - 2\frac{n-1}{n} + \frac{n-1}{n+1} \right) = 2\frac{n}{n+1} \approx \beta^* = 2. \qquad [10]$$

*8. Probability distributions of $\beta$-values* form a family parameterized by the number of elements in the sequence. As shown on Fig. 10, these distributions have a well-defined peak at $\beta_n \approx 2\frac{n}{n+1}$ (see below) and rapidly decay as $\beta$ approaches 1 or for $\beta > 3.5$, which illustrates that typical $\beta$-values, for all $n$, remain near the impartial mean $\beta^* \approx 2$.

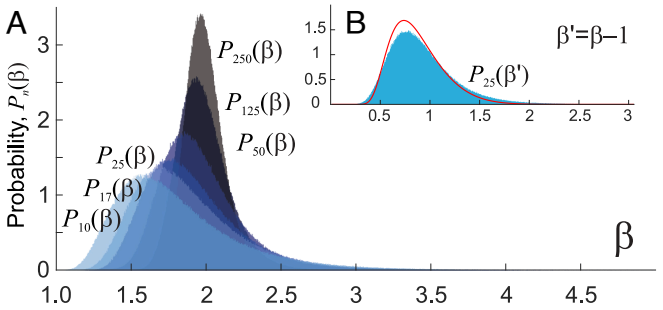


**Fig. 10.** $\beta$-distributions. (*A*) Histograms of $\beta$-values obtained for $10^6$ sequences containing $n = 17$, 25, 50, 125, and 250 elements peak in a vicinity of the impartial mean $\beta^*$ and rapidly decay for $\beta \lesssim 1.2$ and $\beta \gtrsim 3.5$. (*B*) The distribution of $\beta' = \beta - 1$ for sequences containing about $n = 25$ points is close to the universal Kolmogorov distribution $P(\lambda)$ (red line, Fig. 2*A*).

*9. The sliding window algorithm* can be implemented in two ways:

- using a *fixed window* that may capture different numbers of events at each step, i.e., $L_t = L$, but $n_t$ and $n_{t+1}$ may differ;
- using a *fixed number of events* per window, i.e., $n_t = n$, but $L_t$ and $L_{t+1}$ may differ.

In both cases, the mean window width $\bar{L}$ is proportional to the mean separation between nearest events,

$$\bar{l} \equiv \langle l_i \rangle = \langle x_{i+1} - x_i \rangle, \qquad [11]$$

and the mean number $\bar{n}$ of the data points in the sample sequence, $\bar{L} = \bar{l}\bar{n}$. The resulting estimates for $\lambda(t)$ and $\beta(t)$ are nearly identical and, for qualitative assessments, can be used interchangeably.

*10. Local averaging*. To build the dependencies between local averages, we ordered the values assumed by the independent variable, e.g., the speeds, from smallest to largest,

$$\{s_1, s_2, \ldots\} \to \{s'_1 \leq s'_2 \leq \ldots\},$$

subdivided the resulting sequence into consecutive groups containing 100 elements and averaged each set,

$$\hat{s}_i = \frac{1}{100} \sum_{k=-50}^{50} s'_{i+k}.$$

Since each $s_{i_k}$ is associated with a particular moment of time $t_{i_k}$, we computed the averages of the corresponding dependent variable, e.g., $\lambda_{i_k}$,

$$\hat{\lambda}_i = \frac{1}{100} \sum_{k=1}^{100} \lambda_{i_k}.$$

Similarly, ordering the $\beta$-scores and evaluating their local means produces the $\hat{\beta}_i$-values, along with the means of their $\lambda_{i_k}$-counterparts that occur at the corresponding moments $t_{i_k}$.

**Data, Materials, and Software Availability.** Previously published data were used for this work (45). Data files uploaded, sharing URL: https://datadryad.org/stash/share/zchXWoaNFMQhI1b2Qlt3mGgpr3Da09cHJse5ACYwhcU (90).

**ACKNOWLEDGMENTS.** We are grateful to Dr. A. Babichev for fruitful discussions. C.H. and Y.D. are supported by NIH grant R01NS110806 and NSF grant 1901338. C.J. and D.J. are supported by NIH grants R01MH112523 and R01NS097764.

Author affiliations: [a]Department of Neurology, McGovern Medical School, The University of Texas, Houston, TX 77030; [b]Department of Neuroscience, Baylor College of Medicine, Houston, TX 77030; and [c]Department of Molecular and Cell Biology, Baylor College of Medicine, Houston, TX 77030

1. G. Buzsáki, *Rhythms in the Brain* (Oxford University Press, New York, 2011).
2. W. Skaggs, B. McNaughton, M. Wilson, C. Barnes, Theta phase precession in hippocampal neuronal populations and the compression of temporal sequences. *Hippocampus* **6**, 149–172 (1996).
3. K. Bench *et al*., Coherent theta oscillations and reorganization of spike timing in the hippocampal-prefrontal network upon learning. *Neuron* **66**, 921–936 (2010).
4. D. Nikoli, P. Fries, W. Singer, Gamma oscillations: Precise temporal coordination without a metronome. *Trends Cogn. Sci.* **17**, 54–55 (2013).
5. L. Colgin *et al*., Frequency of gamma oscillations routes flow of information in the hippocampus. *Nature* **462**, 353–357 (2009).
6. L. Colgin, E. Moser, Gamma oscillations in the hippocampus. *Physiology* **25**, 319–329 (2010).
7. J. Lisman, G. Buzsáki, A neural coding scheme formed by the combined function of gamma and theta oscillations. *Schizophr. Bull.* **34**, 974–80 (2008).
8. M. Carr, M. Karlsson, L. Frank, Transient slow gamma synchrony underlies hippocampal memory replay. *Neuron* **75**, 700–713 (2012).
9. G. Buzsáki, Theta rhythm of navigation: Link between path integration and landmark navigation, episodic and semantic memory. *Hippocampus* **15**, 827–840 (2005).
10. G. Richard *et al*., Speed modulation of hippocampal theta frequency correlates with spatial memory performance. *Hippocampus* **23**, 1269–1279 (2013).
11. E. Kropff, J. Carmichael, E. Moser, M.-B. Moser, Frequency of theta rhythm is controlled by acceleration, but not speed, in running rats. *Neuron* **109**, 1–11 (2021).
12. P. Fries, A mechanism for cognitive dynamics: Neuronal communication through neuronal coherence. *Trends Cogn. Sci.* **9**, 474–480 (2005).
13. A. Lutz, L. Greischar, N. Rawlings, M. Ricard, R. Davidson, Long-term meditators self-induce high-amplitude gamma synchrony during mental practice. *Proc. Natl. Acad. Sci. U.S.A.* **101**, 16369–16373 (2004).
14. L. Rangel *et al*., Rhythmic coordination of hippocampal neurons during associative memory processing. *eLife* **5**, e09849 (2016).
15. R. Thom, *Structural Stability and Morphogenesis (translated by DH Fowler)* (Benjamin-Addison Wesley, New York, 1975).
16. C. Wilkinson, C. Nelson, Increased aperiodic gamma power in young boys with Fragile X Syndrome is associated with better language ability. *Mol. Autism.* **12**, 17 (2021).
17. T. Donoghue *et al*., Parameterizing neural power spectra into periodic and aperiodic components. *Nat. Neurosci.* **23**, 1655–1665 (2020).
18. T. Eissa *et al*., Multiscale aspects of generation of high-gamma activity during seizures in human neocortex. *eNeuro* **3**, ENEURO.0141-15.2016 (2016).
19. W. Nicola, C. Clopath, A diversity of interneurons and Hebbian plasticity facilitate rapid compressible learning in the hippocampus. *Nat. Neurosci.* **22**, 1168–1181 (2019).
20. S. Hawkins, Situational influences on rhythmicity in speech, music, and their interaction. *Philos. Trans. R. Soc. B.* **369**, 20130398 (2014).
21. A. D. Blanco, R. Ramirez, Evaluation of a sound quality visual feedback system for bow learning technique in violin beginners: An EEG study. *Front. Psychol.* **10**, 165 (2019).
22. S. Cole, B. Voytek, Brain oscillations and the importance of waveform shape. *Trends Cogn. Sci.* **21**, 137–149 (2017).
23. N. Kane *et al*., A revised glossary of terms most commonly used by clinical electroencephalographers and updated proposal for the report format of the EEG findings. Revision 2017. *Clin. Neurophys. Practice* **2**, 170–185 (2017).
24. M. Kural *et al*., Criteria for defining interictal epileptiform discharges in EEG: A clinical validation study. *Neurology* **94**, e2139–e2147 (2020).
25. M. Kural *et al*., Optimized set of criteria for defining interictal epileptiform EEG discharges. *Clin. Neurophys.* **131**, 2250–2254 (2020).
26. U. Will, E. Berg, Brain wave synchronization and entrainment to periodic acoustic stimuli. *Neurosci. Lett.* **424**, 55–60 (2007).
27. H. Mostafa, L. Müller, G. Indiveri, Rhythmic inhibition allows neural networks to search for maximally consistent states. *Neural Comput.* **27**, 2510–2547 (2015).
28. A. Kolmogorov, Sulla determinazione empirica di una legge di distribuzione. *Giornale dell'Istituto Italiano degli Attuari* **4**, 83–91 (1933).
29. M. Stephens, "Introduction to Kolmogorov (1933) on the empirical determination of a distribution" in *Breakthroughs in Statistics. Springer Series in Statistics (Perspectives in Statistics)*, S. Kotz, N. L. Johnson, Eds. (Springer, New York, NY, 1992).
30. V. Arnold, Orbits' statistics in chaotic dynamical systems. *Nonlinearity* **21**, T109 (2008).
31. V. Arnold, Empirical study of stochasticity for deterministic chaotic dynamics of geometric progressions of residues. *Funct. Anal. Other Math.* **2**, 139–149 (2009).
32. V. Arnold, To what extent are arithmetic progressions of fractional parts stochastic? *Russ. Math. Surv.* **63**, 205 (2008).
33. V. Arnold, Stochastic and deterministic characteristics of orbits in chaotically looking dynamical systems. *Trans. Moscow Math. Soc.* **70**, 31–69 (2009).
34. V. Arnold, Measuring the objective degree of randomness of a finite set of points. Lecture at the school "Contemporary Mathematics," (in Russian). Joint Institute for Nuclear Research, Dubna, Ratmino (2009).
35. A. Kolmogoroff, On a new confirmation of Mendel's laws. *Dokl. Akad. Nauk. USSR* **27**, 37–41 (1940).
36. A. Stark, E. A. N. Seneta, Kolmogorov's defence of Mendelism. *Genet. Mol. Biol.* **34**, 177–186 (2011).
37. V. Gurzadyan *et al*., Detecting somatic mutations in genomic sequences by means of Kolmogorov-Arnold analysis. *R. Soc. Open Sci.* **2**, 150143 (2015).
38. V. Gurzadyan, A. Kocharyan, Kolmogorov stochasticity parameter measuring the randomness in the cosmic microwave background. *Astron. Astrophys.* **492**, L33–L34 (2008).
39. O. Brandouy, J.-P. Delahaye, L. Ma, Estimating the algorithmic complexity of stock markets. *Algorithmic Finance* **4**, 159–178 (2015).
40. K. Ford, "From Kolmogorov's theorem on empirical distribution to number theory" in *Kolmogorov's Heritage in Mathematics*, É. Charpentier, A. Lesne, N. K. Nikolski, Eds. (Springer, Berlin, Heidelberg, 2007).
41. V. Arnold, Ergodic and arithmetical properties of geometrical progression's dynamics and of its orbits. *Moscow Math. J.* **5**, 5–22 (2005).
42. V. Arnold, Topology and statistics of arithmetic and algebraic formulae. *Russ. Math. Surv.* **58**, 637–664 (2003).
43. V. Arnold, *Euler Groups and Arithmetics of Geometric Progressions* (MCCME, Moscow, 2003).
44. V. Arnold, *Lectures and Problems: A Gift to Young Mathematicians* (American Math Society, Providence, 2015).
45. J. Cheng, D. Ji, Rigid firing sequences undermine spatial memory codes in a neurodegenerative mouse model. *eLife* **2**, e00647 (2013).
46. S. Ciupek, J. Cheng, Y. Ali, H. Lu, D. Ji, Progressive functional impairments of hippocampal neurons in a tauopathy mouse model. *J. Neurosci.* **35**, 8118–8131 (2015).
47. L. Colgin, Rhythms of the hippocampal network. *Nat. Rev. Neurosci.* **17**, 239–249 (2016).
48. N. Burgess, J. O'Keefe, The theta rhythm. *Hippocampus* **15**, 825–826 (2005).
49. G. Buzsáki, Theta oscillations in the hippocampus. *Neuron* **33**, 325–340 (2002).
50. L. Bol'shev, Asymptotically Pearson transformations. *Theory Proba. Appl.* **8**, 121–146 (1963).
51. J. Vrbik, Small-sample corrections to Kolmogorov-Smirnov test statistic. *Pioneer J. Theor. Appl. Stat.* **15**, 15–23 (2018).
52. J. Vrbik, Deriving CDF of Kolmogorov-Smirnov test statistic. *Appl. Math.* **11**, 227–246 (2020).
53. R. Neamtu *et al*., "Generalized dynamic time warping: Unleashing the warping power hidden in point-wise distances" in *Proceedings of 34th International Conference on Data Engineering (ICDE)* (2018), pp. 521–532.
54. D. Berndt, J. Clifford, "Using dynamic time warping to find patterns in time series" in *Proceedings of the 3rd International Conference on Knowledge Discovery and Data Mining* (AAAI Press, Seattle, WA, 1994), pp. 359–370.
55. S. Salvador, P. Chan, Toward accurate dynamic time warping in linear time and space. *Intell. Data Anal.* **11**, 561–580 (2007).
56. D. Vakman, L. Vainshtein, Amplitude, phase, frequency-Fundamental concepts of oscillation theory. *Sov. Phys. Usp.* **20**, 1002–1016 (1977).
57. S. Rice, Envelopes of narrow-band signals. *Proc. IEEE* **70**, 692–699 (1982).
58. O. Ahmed, M. Mehta, Running speed alters the frequency of hippocampal gamma oscillations. *J. Neurosci.* **32**, 7373–7383 (2012).
59. S. Montgomery, G. Buzsáki, Gamma oscillations dynamically couple hippocampal CA3 and CA1 regions during memory task performance. *Proc. Natl. Acad. Sci. U.S.A.* **104**, 14495–14500 (2007).
60. G. Girardeau, M. Zugaro, Hippocampal ripples and memory consolidation. *Curr. Opin. Neurobiol.* **21**, 452–459 (2001).
61. A. Singer, M. Carr, M. Karlsson, L. Frank, Hippocampal SWR activity predicts correct decisions during the initial learning of an alternation task. *Neuron* **77**, 1163–1173 (2013).
62. L. Roux, B. Hu, R. Eichler, E. Stark, G. Buzsáki, Sharp wave ripples during learning stabilize the hippocampal spatial map. *Nat. Neurosci.* **20**, 845–853 (2017).
63. J. Sadowski, M. Jones, J. Mellor, Sharp-wave ripples orchestrate the induction of synaptic plasticity during reactivation of place cell firing patterns in the hippocampus. *Cell Reps.* **14**, 1916–1929 (2016).
64. E. Denovellis *et al*., Hippocampal replay of experience at real-world speeds. *Elife* **10**, e64505 (2021).
65. C. Barnes, B. McNaughton, S. Mizumori, B. Leonard, L. Lin, Comparison of spatial and temporal characteristics of neuronal activity in sequential stages of hippocampal processing. *Prog. Brain Res.* **83**, 287–300 (1990).
66. X. Wu, D. Foster, Hippocampal replay captures the unique topological structure of a novel environment. *J. Neurosci.* **34**, 6459–6469 (2014).
67. H. Spiers, R. Hayman, A. Jovalekic, E. Marozzi, K. Jeffery, Place field repetition and purely local remapping in a multicompartment environment. *Cerebral Cortex* **25**, 10–25 (2015).
68. D. Nitz, Tracking route progression in the posterior parietal cortex. *Neuron* **49**, 747–56 (2006).
69. A. van Fransen, F. Ede, E. Maris, Identifying neuronal oscillations using rhythmicity. *NeuroImage* **118**, 256–267 (2015).
70. J. von Neumann, E. Wigner, R. Hofstadter, *In the Mathematical Foundations of Quantum Mechanics* attribute a *"great significance"* to the fact that the *"...the general opinion in theoretical physics had accepted the idea that ...continuity ...is merely simulated by an averaging process in a world which in truth discontinuous by its very nature. This simulation is such that man generally perceives the sum of many billions of elementary processes simultaneously, so that the leveling law of large numbers completely obscures the real nature of the individual processes."* (Princeton University Press, Princeton, 1955).
71. F. van Ede, A. Quinn, M. Woolrich, A. Nobre, Neural oscillations: Sustained rhythms or transient burst-events? *Trends Neurosci.* **41**, 415–417 (2018).
72. S. Jones, When brain rhythms aren't 'rhythmic': Implication for their mechanisms and meaning. *Curr. Opin. Neurobiol.* **40**, 72–80 (2016).
73. B. v. Mises, Grundlagen der Wahrscheinlichkeitsrechnung. *Math. Zeitschrift* **5**, 52–99 (1919).
74. V. Uspenskii, A. Semenov, A. Shen', Can an individual sequence of zeros and ones be random? *Russ Math. Surv.* **45**, 105–162 (1990).
75. S. Volchan, What is a random sequence? *Am. Math. Monthly* **109**, 46–63 (2002).
76. H. Berger, Über das Elektrenkephalogramm des Menschen. *Archiv für Psychiatrie und Nervenkrankheiten* **98**, 231–254 (1933).
77. A. Christoph, On some questions of V.I. Arnold on the stochasticity of geometric and arithmetic progressions. *Nonlinearity* **28**, 3663 (2015).
78. M. Weiss, Non-gaussian properties of the EEG during sleep. *Electroencephalogr. Clin. Neurophysiol.* **34**, 200–202 (1973).
79. M. Weiss, Testing EEG data for statistical normality. Images of the twenty-first century. *Proc. Ann. Int. Eng. Med. Biol. Soc.* **2**, 704–705 (1989).
80. M. Weiss, Testing correlated "EEG-like" data for normality using a modified Kolmogorov-Smirnov statistic. *IEEE Trans. Biomed. Eng.* **33**, 1114–20 (1986).
81. J. McEwen, G. Anderson, Modeling the stationarity and Gaussianity of spontaneous electroencephalographic activity. *IEEE Trans. Biomed. Eng.* **22**, 361–369 (1975).
82. Y. Greenstein, C. Pavlides, J. Winson, Long-term potentiation in the dentate gyrus is preferentially induced at theta rhythm periodicity. *Brain Res.* **438**, 331–334 (1988).
83. M. Hinder *et al*., Inter- and intra-individual variability following intermittent theta burst stimulation: Implications for rehabilitation and recovery. *Brain Stimul.* **7**, 365–371 (2014).
84. J. Larson, E. Munkácsy, Theta-burst LTP. *Brain Res.* **1621**, 38–50 (2015).

85. G. Sheridan, E. Moeendarbary, M. Pickering, J. O'Connor, K. Murphy, Theta-burst stimulation of hippocampal slices induces network-level calcium oscillations and activates analogous gene transcription to spatial learning. *PLoS One* **9**, e100546 (2014).
86. P. Nguyen, E. Kandel, Brief theta-burst stimulation induces a transcription-dependent late phase of LTP requiring cAMP in area CA1 of the mouse hippocampus. *Learn. Memory* **4**, 230–243 (1997).
87. M. Lundqvist *et al.*, Gamma and beta bursts underlie working memory. *Neuron* **90**, 152–164 (2016).
88. A. Babichev, D. Morozov, Y. Dabaghian, Replays of spatial memories suppress topological fluctuations in cognitive map. *Net. Neurosci.* **3**, 1–18 (2019).
89. P. Aleksandrov, *Elementary Concepts of Topology* (F. Ungar Publishing, 1965).
90. J. Cheng, D. Ji, Pattern dynamics and stochasticity of the brain rhythms. Dryad. https://datadryad.org/stash/share/zchXWoaNFMQhI1b2Qlt3mGgpr3Da09cHJse5ACYwhcU. Deposited 9 March 2023.